Development of a meso-microscale coupling procedure for site assessment in complex terrain

F. A. Castro[1], C. Silva Santos[1,2], J. C. Costa[1]

[1] Instituto Superior de Engenharia do Porto
Rua Dr António Bernardino de Almeida, 431, 4200-072 Porto, Portugal (tel. +351228340500)
fac@isep.ipp.pt, loc@isep.ipp.pt
[2] Megajoule Inovação
Rua Eng. Frederico Ulrich, 2650, 4470-605 Maia, Portugal (tel. +351220915480)
carlos.santos@megajoule.pt

Abstract. A procedure for coupling mesoscale and CFD codes is presented, enabling the inclusion of realistic stratification flow regimes and boundary conditions in CFD simulations of relevance to site and resource assessment studies in complex terrain. Two distinct techniques are derived: (i) in the first one, boundary conditions are extracted from mesoscale results to produce time-varying CFD solutions; (ii) in the second case, a statistical treatment of mesoscale data leads to steady-state flow boundary conditions believed to be more representative than the idealised profiles which are current industry practice. Results are compared with measured data and traditional CFD approaches.

1 Introduction

The use of CFD techniques for site assessment permits the capturing of important flow aspects not in reach of either linear or mesoscale models. If, on one hand, linear models are incapable of accurately capturing non-linear phenomena, such as flow separation, on the other, mesoscale simulations cannot cope with the high spatial resolutions necessary to resolve small, yet often crucial, flow features occurring near turbine locations.

However, it is our belief that the performance of CFD in the wind energy industry has been impaired by the use of synthetic, idealised, boundary conditions, describing often unrealistic flow and regime conditions for the sites under study.

In this work, we propose to use mesoscale simulations to obtain more appropriate boundary conditions for CFD. We believe that this approach brings two main advantages: (i) the resulting boundary conditions are more representative of local terrain conditions than the usual idealised profiles and (ii) a wider range of stratification regimes can be considered and their individual effects accounted for.

To accomplish this task, the WINDIE^{TM} CFD code was developed in-house with the capability to simulate non-neutral flows over complex terrain. For that purpose, a potential temperature transport equation was added to a URaNS code. Several turbulence models are available whose performance is under study.

The CFD simulations are driven by boundary conditions which are interpolated from mesoscale results onto the CFD mesh. In the most fundamental form of the technique, those boundary conditions are time-varying flow fields which produce a time-varying CFD simulation similar to, but with much higher resolution than, the mesoscale case. This first approach is ideal to investigate specific phenomena occurring during short periods of, say, a month, since its computational cost precludes its use for the simulation of a year-long flow without large computational resources. A second approach, closer to the common industry practice, involves the statistical treatment of mesoscale fields to produce a steady-state flow condition. It is believed that this will represent an enhancement to the typical synthetic boundary conditions currently used in site assessment procedures using CFD.

The described approaches will be applied to two sites of different complexity, providing a framework for the evaluation for the proposed techniques. For the first approach, results of transient simulations will be compared against measured time series, whilst in the second approach a comparison will be made with traditional CFD site assessment strategies.

2 Numerical Techniques

In this section, the numerical techniques used in the simulations of the mesoscale and CFD microscale codes are presented.

2.1 Mesoscale WRF code

In this work we use the 3.1.1 version of the Weather Research and Forecasting Model with Advanced Research WRF solver (WRF-ARW). The WRF-ARW code was built using the `real` compilation option. The TKE 1.5 diffusion model was used in all simulations to be able to compare turbulent kinetic energy derived quantities with equivalent experimental and CFD numerical results. The WRF-ARF boundary conditions were extracted from the NCEP FNL Operational Model Global Tropospheric Analyses.

2.2 CFD code

The core of the present Unsteady Reynolds averaged Navier-Stokes (URaNS) CFD code was developed in [1] for the simulation of neutral atmospheric flows over complex terrain. Here it is extended to include stratification and rotational effects (Coriolis fictitious force). The code was parallelized, to reduce execution time, using the same techniques of [2].

Mathematical model The code uses the anelastic, Boussinesq and Reynolds averaged Navier-Stokes approximations of the fundamental equations for fluid dynamics. Written in tensor notation for a generic coordinate system, the continuity, momentum and energy (dry potential temperature) equations are,

$$\frac{\partial \left(\rho U_j \beta_k^j\right)}{\partial \xi^j} = 0, \tag{1}$$

$$J\rho\frac{\partial U_i}{\partial t} + \rho\frac{\partial}{\partial \xi^j}\left(U_k U_i \beta_k^j\right) = -\frac{\partial}{\partial \xi^j}\left(p'\beta_i^j\right) + \frac{\partial}{\partial \xi^j}\left[\sigma_{ki}\beta_k^j\right] + Jf\epsilon_{ij3}U_j - J\rho' g\delta_{i3}, \tag{2}$$

$$J\rho\frac{\partial \theta}{\partial t} + \rho\frac{\partial}{\partial \xi^j}\left(U_k \theta \beta_k^j\right) = \frac{\partial}{\partial \xi^j}\left[\frac{1}{J}\frac{\mu_t}{Pr}\frac{\partial \theta}{\partial \xi^m}\beta_k^m\beta_k^j\right], \tag{3}$$

respectively, with,

$$\sigma_{ij} = -\frac{2}{3}\rho k\delta_{ij} + \frac{\mu_t}{J}\left(\frac{\partial U_i}{\partial \xi^m}\beta_j^m + \frac{\partial U_j}{\partial \xi^m}\beta_i^m\right), \tag{4}$$

where ρ is the fluid density of a background hydrostatic reference state, $U_i = (u, v, w)$ the mean velocity vector, p' and ρ' the pressure and density perturbations to the background hydrostatic reference state, g the magnitude of gravity acceleration, f the Coriolis parameter, θ the dry potential temperature, k the turbulent kinetic energy, μ_t the turbulent eddie viscosity and Pr the turbulent Prandtl number.
The terrain-following coordinate system is defined by transforming a physical Cartesian coordinate system into a computational system ($x_i \mapsto \xi^i$), where $\beta_k^j = J\partial\xi^j/\partial x^k$ and J are the co-factors and the determinant of the Jacobian matrix of the coordinate transformation [3]. This transformation makes it relatively simple to treat the boundary conditions and to use a structured mesh, where the physical domain boundaries are the coordinate surfaces following the topography. For all the simulations, the Coriolis parameter was $f = 2\Omega\sin(\varphi) \simeq 1 \times 10^{-4}$ s^{-1}, corresponding to a latitude of $\varphi \simeq 40^\circ$ (earth's rotation $\Omega = 0.76 \times 10^{-4}$ s^{-1}).
Four turbulence models were evaluated, namely three flavours of the $k-\varepsilon$ turbulence model of [4] and a one equation TKE turbulence model, similar to that used in the WRF-ARW code (see [5]).
Among the three flavours of the $k-\varepsilon$ turbulence model two of them correspond to two different constant sets of the standard model of [4] while the other is the RNG $k-\varepsilon$ turbulence model (see e.g. [6, 7]).
All the turbulence models evaluated here shared the same transport equation for the turbulent kinetic energy (k). Using a generic coordinate system,

$$J\rho\frac{\partial k}{\partial t} + \rho\frac{\partial}{\partial \xi^j}\left(U_k k \beta_k^j\right) = \frac{\partial}{\partial \xi^j}\left[\frac{1}{J}\frac{\mu_t}{\sigma_k}\frac{\partial k}{\partial \xi^m}\beta_k^m\beta_k^j\right] + J\left(P_k + S_k - \rho\varepsilon\right), \tag{5}$$

where ε represents the dissipation rate of k, σ_k is a model constant, and

$$P_k = \sigma_{ij}\frac{1}{J}\frac{\partial U_i}{\partial \xi^m}\beta_j^m, \; S_k = -\frac{1}{J}\frac{g\mu_t}{\theta_0 Pr}\frac{\partial \theta}{\partial \xi^m}\beta_m^3 \tag{6}$$

are the mechanical and thermal production/destruction source terms, respectively. The potential temperature is denoted by θ_0, while the subscript 0 refers to a thermodynamic reference state.
In the case of the one equation TKE 1.5 model, ε was modelled as (see [5]),

$$\varepsilon = \frac{Ck^{3/2}}{\ell}, \tag{7}$$

Table 1: Turbulence model contants. C_{1R} derived from (15)

	STND	Atmos	RNG
C_μ	0.09	0.033	0.085
C_1	1.44	1.46	C_{1R}
C_2	1.92	1.83	1.68
σ_k	1.0	1.0	0.7179
σ_ε	1.3	2.38	0.7179

with

$$C = 1.9C_k + \frac{0.93 - 1.9C_k}{\Delta s}\ell, \tag{8}$$

with C_k a model constant ($C_k = 0.075$ in all simulations) and $\Delta s = (\Delta x \Delta y \Delta z)^{1/3}$. The characteristic length is

$$\ell = \min\left[\Delta s,\, 0.76\sqrt{k}/N\right], \tag{9}$$

where the Brunt–Väisälä frequency N is calculated from

$$N^2 = \frac{g}{\theta}\frac{\partial \theta}{\partial z}. \tag{10}$$

The eddy viscosity is obtained from

$$\mu_t = \rho C_k \ell \sqrt{k}, \tag{11}$$

where the characteristic length ℓ was calculated using

$$\ell = \begin{cases} \min\left[\Delta s,\, 0.76\sqrt{k}/N\right], & N^2 > 0 \\ \Delta s, & N^2 < 0. \end{cases} \tag{12}$$

For all the $k - \varepsilon$ turbulence model flavours evaluated here, a turbulent kinetic energy dissipation rate (ε) transport equation of the form,

$$J\rho\frac{\partial \varepsilon}{\partial t} + \rho\frac{\partial}{\partial \xi^j}\left(U_k \varepsilon \beta_k^j\right) = \frac{\partial}{\partial \xi^j}\left[\frac{1}{J}\frac{\mu_t}{\sigma_\varepsilon}\frac{\partial \varepsilon}{\partial \xi^m}\beta_k^m \beta_k^j\right] + J\frac{\varepsilon}{k}\left(C_1\left(P_\varepsilon + S_k\right) - C_2\rho\varepsilon\right), \tag{13}$$

was used, enabling, in conjunction with k, the estimation of a eddy viscosity field, given by

$$\mu_t = \rho C_\mu k^2/\epsilon. \tag{14}$$

For all turbulence models here, $P_\varepsilon = P_k$.
Two different constant sets of the standard model of [4] were tested. They are the first two sets of table 1, designated by Stnd and Atmos respectively, and they follow from the use of two different C_μ values. The Stnd value corresponds to the original value of the model of [4] and the Atmos variant results from analysis of several atmospheric surface layer results (see e.g. [8] and references therein).
In case of the RNG $k - \varepsilon$ variant of [6], C_1 is no longer a constant, being obtained by,

$$C_{1R} = C_1 - \eta\frac{1 - \eta/4.38}{1 + 0.015\eta^3}, \tag{15}$$

with

$$\eta = \frac{k}{\varepsilon}\sqrt{2S_{ij}S_{ij}}, \tag{16}$$

where

$$S_{ij} = \frac{1}{2}\left(\frac{\partial U_i}{\partial x_j} + \frac{\partial U_j}{\partial x_i}\right), \tag{17}$$

is the mean field strain rate tensor written in a Cartesian coordinate system. In equation (15) $C_1 = 1.44$, the standard value.

Boundary conditions It will be necessary to describe two families of boundary conditions: those used in the coupled and non-coupled CFD simulations. Nevertheless, some formulations are shared between these two types, namely some parts of the ground boundary condition.
The first grid node above the bottom boundary is always well inside the surface layer, enabling the use of boundary conditions following the Monin-Obukov similarity theory. In both coupled and non-coupled formulations, the momentum equations are modified to include a Reynolds shear stress at the bottom boundary, following the relation,

$$\frac{\tau_{wall}}{\rho} \equiv u_*^2 = k^{1/2} C_\mu^{1/4} \frac{U_\parallel \kappa}{\ln(1 + z/z_0) + \psi_m}, \tag{18}$$

irrespective of the turbulence model under use. Here z is the height above ground level of the control volume centre adjacent to the boundary, z_0 is the characteristic roughness, $U_\parallel$ is the velocity parallel to the boundary at height z, κ is the von KÂ·rmÂ·n constant (used $\kappa = 0.4$) and ψ_m is the Businger-Dyer diabatic correction for momentum, calculated using (see [9])

$$\psi_m = \begin{cases} 4.7\frac{z}{L}, & L \geq 0 \\ -2\log(\frac{1}{2}(1+\zeta)) - \log(\frac{1}{2}(1+\zeta^2)) + 2\arctan(\zeta) - \frac{\pi}{2}, & L < 0, \end{cases} \tag{19}$$

with $\zeta = (1 - 15\frac{z}{L})^{1/4}$, resulting from the integration of the Businger-Dyer momentum functions,

$$\phi_m = \begin{cases} 1 + 4.7\frac{z}{L}, & L \geq 0 \\ \left(1 - 15\frac{z}{L}\right)^{-1/4}, & L < 0. \end{cases} \tag{20}$$

The Monin-Obukov length L is defined by

$$L = -\frac{u_*^3 \theta}{g\kappa(\overline{w'\theta'})_0}, \tag{21}$$

where $(\overline{w'\theta'})_0$ represents the turbulent heat flux at the ground.
For the TKE 1.5 model, where there is no C_μ model parameter, the Reynolds Shear stress is calculated using equation (18) for a target $C_\mu^{1/2} = 0.033^{1/2}$.
In case of the dry potential temperature transport equation (energy equation), used only in the coupled simulations, the turbulent heat flux at the bottom boundary is obtained from the WRF simulation results, being available as a time varying quantity. The WRF heat flux is linearly interpolated in space for the CFD mesh positions and then linearly interpolated in time from two consecutive WRF output frames (20 minutes interval).
The ground boundary conditions used in the turbulence models follow the principle of local equilibrium between mechanical production, dissipation and thermal production/dissipation (when applicable) and assume that the first control volume is well inside the surface layer, where the Reynolds shear stress is considered almost constant ($\tau \simeq \tau_{wall} \equiv \rho u_*^2$). For this prototype behaviour the kinetic energy dissipation rate ε is approximated using,

$$\varepsilon = u_*^3 \left(\frac{\phi_m}{\kappa z} - \frac{1}{\kappa L} \right). \tag{22}$$

For the coupled CFD simulations, the lateral and top boundary conditions were obtained from WRF results (simulations performed in advance), using tri-linear interpolation in space and linear interpolation in time, between two consecutive output WRF frames (20 minutes interval). The interpolated quantities were the velocity components u_i, the potential temperature θ and the reference state density ρ. For each WRF output frame, a density and potential temperature CFD reference state was constructed. The turbulent quantities (k, ε) were not subjected to time-varying Dirichlet boundary conditions. The adopted boundary condition for those quantities was linear extrapolation of the interior fields.
For the coupled CFD simulations, relaxation regions adjacent to the lateral and top boundaries were used to help enforce the boundary conditions, without spurious wave reflections. These zones follow the sponge layer formulation used in [10] and were applied only to the velocity and temperature fields.
Because the topography description used in the CFD and WRF simulations need not be the same, a procedure was adopted to force the WRF topography at the lateral boundaries of the CFD mesh and promote a smooth transition to the CFD topography within a layer of specified thickness. This procedure is based on the work of [11].
In the case of the non-coupled CFD simulations, which are always performed for a neutral stratification regime, the inflow boundary conditions were obtained by specifying an inlet logarithmic profile, of the form,

$$u = \frac{u_*}{\kappa} \ln\left(1 + \frac{z}{z_0}\right), \tag{23}$$

and a turbulent field,

$$k = \begin{cases} u_*^2/C_\mu^{1/2}\,(1 - z/\delta)\,, & z \leq 0.99\delta \\ u_*^2/(100C_\mu^{1/2}), & z > 0.99\delta, \end{cases} \tag{24}$$

$$\varepsilon = \begin{cases} C_\mu^{3/4}k^{3/2}/(\kappa z), & z \leq 0.95\delta \\ C_\mu^{3/4}k^{3/2}/(0.95\delta\kappa), & z > 0.95\delta, \end{cases} \tag{25}$$

where δ is a prescribed boundary layer height. It was considered that the velocity field was always tangential at the top and lateral boundaries. The velocity outflow condition was obtained by linear extrapolation from the inner nodes, constrained by global mass conservation. As in the case of coupled CFD simulations, the turbulent quantities (k, ε) were obtained from linear extrapolation from the interior fields.
For all simulations, coupled and non-coupled, the pressure field on all boundaries was obtained from linear extrapolation from the interior fields.

3 Time-varying meso-microscale coupling procedure

In this section, we present the results for time dependent simulations of both CFD and WRF codes, produced for a moderately complex site, designated by S1, with a mean RIX factor of 21.8%.
The main objective of this experiment is to determine the extent to which the coupled CFD code can adequately reproduce the dynamical meteorological behaviour observed in the experimental results of the horizontal velocity magnitude and direction (V_h, ϕ) and horizontal turbulence intensity (I_u). It is believed that a good representation of the low altitude dynamic behaviour of the atmospheric flow is an important requisite to a successful coupling of meso and microscale codes, even though the main objective here is to have an efficient stationary coupling for site and resource assessment purposes.
Some preliminary WRF simulations were performed to determine the horizontal spatial resolution to be used. A mesh of 88 $\times$ 88 $\times$ 31 grid nodes, using $\Delta x = \Delta y = 3000$ m emerged as a good compromise, offering acceptable results and using a common setup in mesoscale applications.
Coupled CFD simulations were performed using a domain of $\sim$ 32 km $\times$ 32 km using a mesh of 40 $\times$ 40 $\times$ 51 grid nodes, centred on a meteorological station position, where the mesh has minimum horizontal grid dimensions of $\Delta x = \Delta y \sim$ 400 m. In the vertical the mesh was concentrated near the bottom boundary, where the first node was placed 2 m above ground level, reaching an absolute height of 7500 m at the top boundary. The URaNS equations were integrated in time using an implicit three time scheme using a $\Delta t = 2$ s time step. The mesh dimensions and time step enabled a typical simulation of 5 days to be concluded in nearly 10 h wall clock, when using a domain decomposition of 9 domains (3×3) and running in a 8 cores Xeon Intel@2.8 GHz processors machine. Coupled CFD simulations were performed for several periods across the available time window of the measurements campaign, for typical periods of about 5 days. Here we only present results for two of these periods, one in November 2007 and the other in April 2008, covering two different seasons.
Figures 1 and 2 show time series for the horizontal velocity (V_h) and turbulence intensity (I_u), defined by,

$$I_u \equiv \frac{\sigma_u}{V_h} = \frac{\sqrt{\frac{4}{3}k + 2\mu_t\frac{\partial w}{\partial z}}}{V_h}, \tag{26}$$

for 5 days in November 2007, enabling the comparison between the numerical CFD and WRF simulations results with the cup anemometer measurements (CUP). The first conclusion that may be drawn is that the turbulence models do not have a large influence on V_h. The only occasion where the several results show some noticeable difference was around 3.6 days into the simulated period, when the flow reached almost a stagnant state which enhanced the diffusion role in the establishment of the flow. Overall the CFD results follow qualitatively well the measured data with significantly better results than the mesoscale prediction. In terms of mean horizontal velocity, the WRF results predicted a value of $V_h = 6.4$ m/s which compares poorly with the measured mean velocity of $V_h = 8.6$ m/s, i.e. -26% error. By contrast, through the coupling procedure, WINDIE™ yielded a much more accurate mean velocity of $V_h = 8.4$ m/s (-3% error).
The I_u results present a better opportunity for the appraisal of the turbulence models. From figure 2, it can be seen that the RNG model produced almost always lower turbulence intensity levels. The STND model, although efficient at capturing some of the turbulence peaks that typically occurred around noon, produced lower turbulence intensity levels during the night. Because of these behaviours, the following results were obtained using the $k - \varepsilon$ Atmos and TKE 1.5 turbulence models.

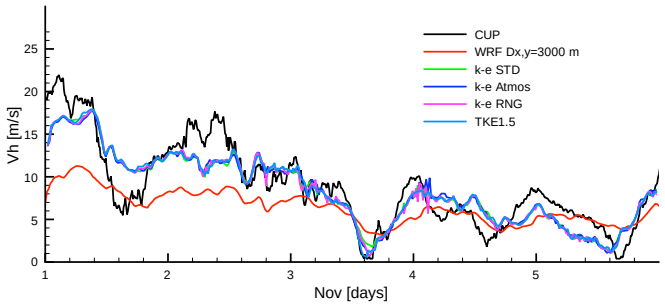

Fig. 1: Horizontal velocity time series for first days of a November month at 60 m agl for site 1. Cup anemometer, WRF and CFD results for different horizontal mesh resolutions.

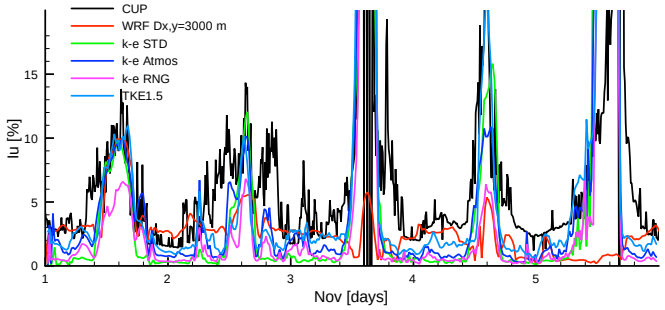

Fig. 2: Horizontal turbulent intensity time series for first days of a November month at 60 m agl for site 1. Cup anemometer, WRF and CFD results for different horizontal mesh resolutions.

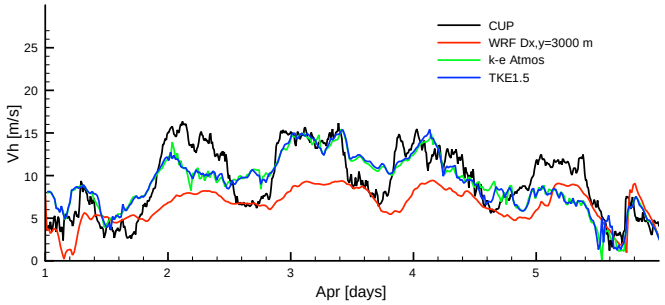

Fig. 3: Horizontal velocity time series for first days of a April month at 60 m agl for site 1. Cup anemometer, WRF and CFD results for different horizontal mesh resolutions.

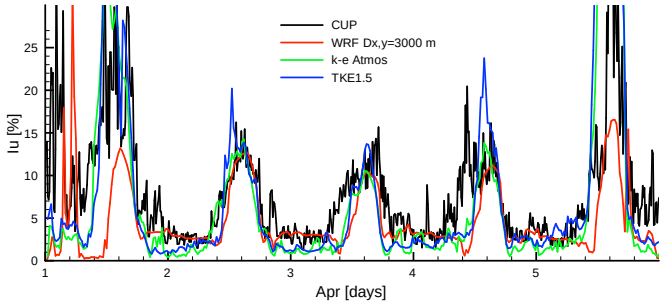

Fig. 4: Horizontal turbulent intensity time series for first days of a April month at 60 m agl for site 1. Cup anemometer, WRF and CFD results for different horizontal mesh resolutions.

Table 2: Results of time-varying coupling simulations

Period	CUP	WRF			WINDIE™		
	$\bar{V_h}$ [m/s]	$\bar{V_h}$ [m/s]	RMS [m/s]	$\bar{V_h}$ error	$\bar{V_h}$ [m/s]	RMS [m/s]	$\bar{V_h}$ error
Nov 2007	**8.6**	**6.4**	2.93	-26%	**8.4**	1.80	-3%
Apr 2008	**9.6**	**6.7**	3.24	-30%	**9.4**	2.09	-3%

Another experiment, performed for an April month, is presented in figures 3 and 4. These Spring results show a more marked diurnal cycle, with higher velocity nocturnal events followed by calmer winds during the day, accompanied with larger turbulence intensity episodes of thermal origin.
The velocity predicted by the WRF code was almost always below the measurements, a situation improved by the WINDIE™ CFD code (figure 3). Once again the V_h CFD results were very similar for all turbulence models but the I_u results showed a greater tendency for the TKE1.5 model to produce higher peaks of turbulence.
In terms of mean horizontal velocity, (see table 2), results evidence once more the marked improvement introduced by the coupling technique: while WRF results produced a $V_h = 6.7$ m/s, well below the measured result of $V_h = 9.6$ m/s (-30%), the WINDIE™ result of $\bar{V_h} = 9.4$ m/s incurred an error of only -3%, i.e. one order of magnitude lower.
A large number of other occasions were simulated (not shown here) and the overall conclusion that can be drawn is that the CFD code can simulate with an interesting degree of realism the meteorological behaviour of both the velocity and turbulence intensity fields. In many occasions, the CFD was seen to improve to a large degree the results produced by the WRF simulations (mainly velocity). However, in some others, the WRF results were already of such high quality that the CFD results could only follow, and even occasionally slightly worsen, the WRF prediction. Nevertheless, taking into account all cases performed so far, the overall picture points to a definite improvement in results brought about by the coupling procedure.
From these experiments we conclude that the proposed coupling procedure can realistically reproduce the low altitude dynamic meteorological fields of velocity and turbulence strongly suggesting that it may be used to produce an enhanced version of the traditional site and resource assessment procedures using CFD. These traditional tools typically use synthetic and simplified boundary conditions, where the flow is normally restricted to leave the domain by one boundary and without a pragmatic way of using (or specifying) non-neutral stratification regimes. The presentation of this enhanced tool will be performed in the following section.

4 Steady-state meso-microscale coupling procedure

To evaluate the performance of the coupling procedure for a typical site assessment project another site was used. The new site, site S2 presented in figure 5, has medium complexity, with a mean RIX value above 20%. During a period of almost 2 years four meteorological towers equipped with cup anemometers and wind vanes measured simultaneously at 80 m agl (see figure 5).
To generate boundary conditions for the CFD code, a mesoscale simulation ofthe year 2006 was performed using WRF. The WRF results were then directionally filtered to produce average directional results at the reference location, chosen to be the second location starting the counting from the south side of the park (see figure 5).
Based on the wind roses for the reference location, obtained from the CUP anemometer results and WRF simulation and presented at figure 6, it was decided to simulate the two northern more frequent sectors, the 0° and 330° sectors.
From figure 6 it can be seen that the WRF results captured fairly well the directional wind distribution at the reference location. That was not the case for the northern tower locations (not shown) were the coarse mesh resolution used in the WRF simulation was not as efficient in capturing the terrain complexity.
Two sets of CFD simulations were performed, using the new coupled procedure and the traditional synthetic boundary conditions procedure. The simulation domains covered square areas of about 17 $\times$ 17 km, cent red at the reference location, with the top boundary placed at an altitude of 6.5 km. For these domains, meshes of $89\times89\times65$ grid nodes were used. The minimum distance between grid nodes was 80 m in the horizontal directions, around the reference point, and 1 m away from the ground in the vertical direction. The grids expanded geometrically in all directions.
For the two target wind sectors, 330° and 0° wind sectors, steady-state solutions were obtained using the two simulation procedures. In case of the synthetic boundary conditions procedure the mesh was always rotated to align the direction of the flow with the positive x direction of the computational mesh, whereas

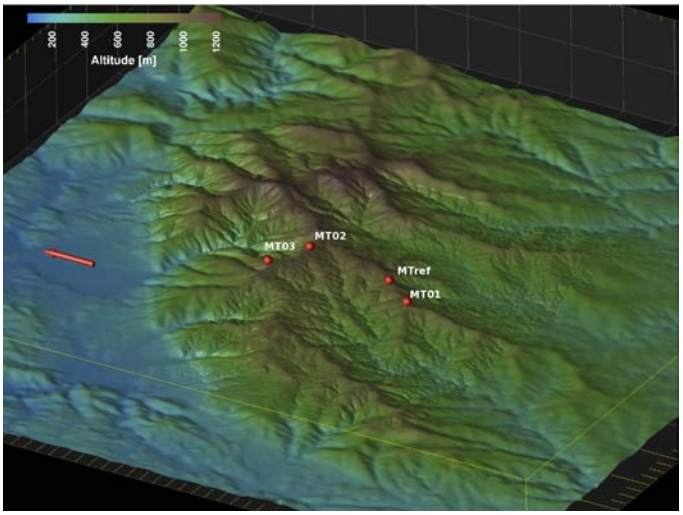

Fig. 5: Three-dimensional representation of the topography at site S2. Red dots mark the locations of the meteorological masts. Red arrow points to North.

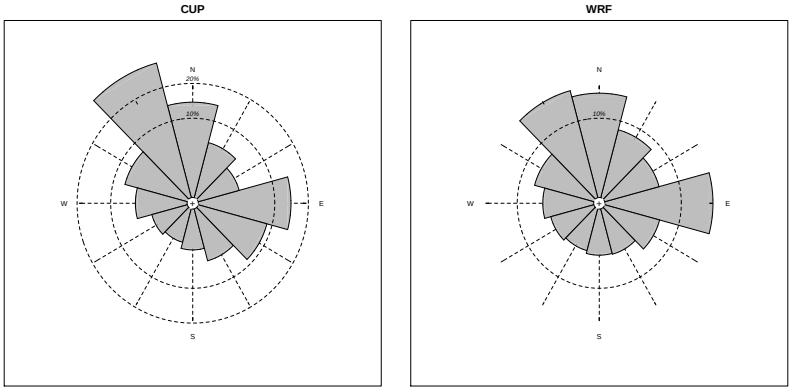

Fig. 6: Wind Roses for the reference location; experimental results left, WRF right.

in the coupled procedure the mesh was not rotated, being positioned such as to align the geographic north-south axis with the negative y-direction. The results presented here only focus on the horizontal mean wind field and, in particular, on the wind velocity ratios between meteorological towers.

As an example of the difference in global results obtained using the two formulations, three-dimensional representations of the two flows are presented in figures 7 and 8 for the 0° wind direction.

Immediately noticeable from the results of figures 7 and 8 is the wind rotation with height observable in the results from the coupled approach. This is a well known characteristic of the atmospheric flows that results from the Coriolis fictitious forces, not present in the results from the traditional approach. In general, the use of synthetic boundary conditions compels the flow to be directionally homogeneous, a feature than many times generates numerical problems near the lateral boundaries, when the latter promote a tendency for the flow to leave or enter de domain. To alleviate these problems it is sometimes necessary to artificially smooth the topography near the boundaries or sometimes increase the simulation domain to conveniently separate these numerical articial features from the area under study.

It is also evident from figure 7 that the coupled procedure enabled the modelling of wave activity, visible in the colour patterns of the w velocity component distribution presented in the vertical plane. This wave activity is a result of the stratified mean flow produced by the WRF results, that is absent in the neutrally stratified simulations performed with the traditional approach. The impact of the stratification in flows over complex terrain is well known (see for example [12]) and the possibility of adequately incorporating this forcing in WINDIE^{TM} is an enormous advantage of the present coupled procedure.

The horizontal mean wind field velocity ratios between meteorological towers are presented in table 3 for the two studied wind flow directions.

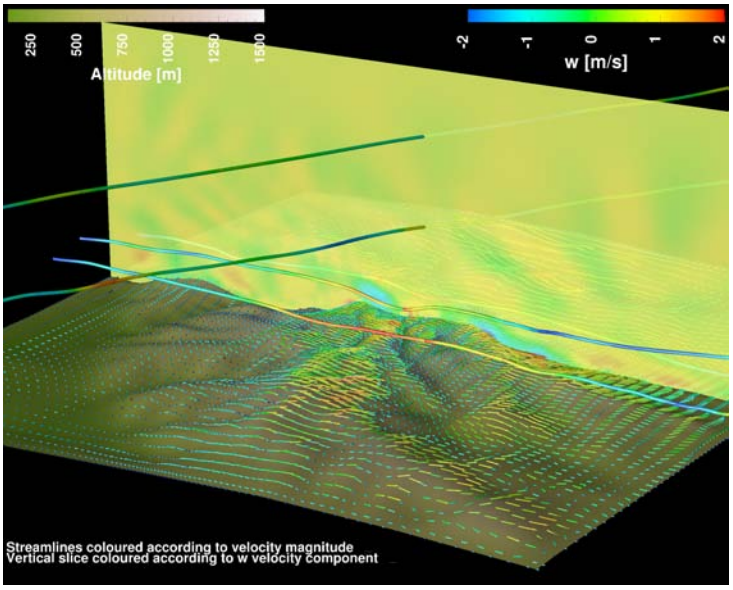

Fig. 7: Flow representation for winds from the North sector at reference station. Vertical plane showing where colors represent isovales of vertical velocity w. Results obtained used de coupled procedure.

Table 3: Comparison between measured velocity ratios at met stations and those obtained with the two CFD approaches.

0°	Measurements	Traditional Approach	Coupled Approach
MT01 vs MTRef	1.00	0.49 (-51%)	0.95 (-5%)
MT02 vs MTRef	0.77	1.40 (+63%)	0.77 ($\pm$0%)
MT03 vs MTRef	0.62	1.15 (+53%)	0.60 (-2%)
330°	Measurements	Traditional Approach	Coupled Approach
MT01 vs MTRef	0.97	1.11 (+14%)	0.77 (-21%)
MT02 vs MTRef	0.85	1.08 (+27%)	0.70 (-18%)
MT03 vs MTRef	0.67	1.02 (+52%)	0.60 (-33%)

From table 3 it can be seen that the coupled procedure performed very well for the 0° wind flow and less well for 330°. In both cases the results are better when using the coupled procedure. A linear estimate of the overall error for both approaches lead to 44% for the traditional technique and 13% for the coupled one. No specific tuning was performed for either technique and these errors could easily be reduced if a series of refinements tests were conducted. This lack of tuning was intended as a way to observe the fundamental differences of the two approaches. It is also be noted that these values correspond to individual simulations, and that a complete site and resource assessment study would involve a complete set of directional simulations with subsequent averaging and error reductions.

5 Conclusion

A meso-microscale coupled procedure was developed to enhance the quality and physical consistency of numerical site assessment studies. To obtain a well established procedure with solid physical support, the coupling procedure was first developed to produce time-varying solutions for atmospheric flows and so enable the direct comparison with time series from meteorological instruments and numerical mesoscale simulations. This first task, acting here as as validation of the numerical procedure, produced very encouraging results, leading to the conclusion that the proposed coupling procedure can realistically reproduce the low altitude dynamic meteorological fields of velocity and turbulence and so gather the theoretical optimal requisites to produce an enhanced version of the traditional site assessment CFD procedures – those that use synthetic and simplified boundary conditions, where the flow is normally restricted to leave the domain by one boundary and without a pragmatic way of using (or specifying) non neutral stratification regimes.

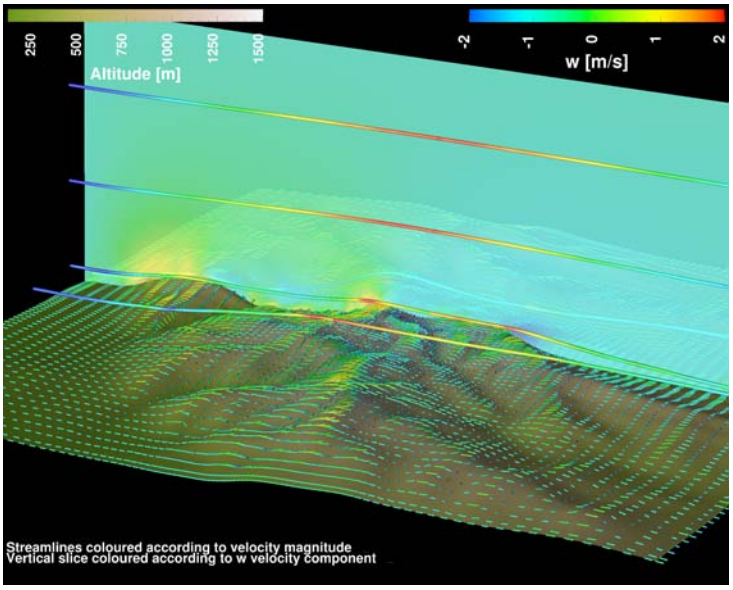

Fig. 8: Flow representation for winds from the North sector at reference station. Vertical plane showing where colors represent isovales of vertical velocity w. Results obtained used the traditional procedure using synthetic boundary conditions.

Year long mesoscale results were then generated to produce directionally averaged results to couple with the CFD code. The results obtained with this procedure supplanted those from the traditional approach. A simple estimated of the mean error obtained in the prediction of velocity ratios showed errors almost 3 times smaller for the new coupled procedure. The error *per se* could be considered not small, but it should be brought in mind that no specific simulations tuning was performed.
The technique is still in a development stage and a large set of tests still remain to complete our validation task list. Nevertheless, the present results indicate that the technique has the potential to increase the accuracy of site and resource assessment studies using WINDIE^{TM} and bring about a reduction in the uncertainty of these results.

References

1. F. A. Castro. *Numerical Methods for the Simulation of Atmospheric Flows over Complex Terrain (in Portuguese)*. PhD thesis, Faculty of Engeneering of Porto, 1997.
2. F. A. Castro, C. S. Santos, and J. M. L. M. Palma. Parallelisation of the CFD Code of a CFD-NWP Coupled System for the Simulation of Atmospheric Flows over Complex Terrain. *High Performance Computing for Computational Science - VECPAR 2008*, pages 27–38, 2008.
3. P. Knupp and S. Steinberg. *Fundamentals of grid generation*. CRC Press, 1994.
4. W. P. Jones and B. E. Launder. The prediction of laminarization with a two-equation model of turbulence. *International Journal of Heat and Mass Transfer*, 15:301–314, 1972.
5. W. C. Skamarock, J. B. Klemp, J. Dudhia, D. O. Gill, D. M. Barker, M. G. Duda, X. Huang, W. Wang, and J. G. Powers. A description of the advanced research wrf version 3. *NCAR TECHNICAL NOTE, NCAR/TN–475+STR*, 2008.
6. V. Yakhot and S. A. Orszag. Renormalization group analysis of turbulence. i. basic theory. *J. Scientific Computations*, 1:3–51, 1986.
7. H.G. Kim and V.C. Patel. Test of turbulence models for wind flow over terrain with separation and recirculation. *Boundary-Layer Meteorology*, 94(1):5–21, Jan 2000.
8. P. G. Duynkerke. Application of the e-ε turbulence closure model to the neutral and stable atmospheric boundary layer. *Journal of the Atmospheric Sciences*, 45(5):865–880, 1988.
9. R. B. Stull. *An Introduction to Boundary Layer Meteorology*. Kluwer Academic Publishers, 1988.
10. D. R. Durran and J. Klemp. A compressible model for the simulation of moist mountain waves. *Monthly Weather Review*, Jan 1983.
11. K. J. Eidsvik, A. Holstad, I. Lie, and T. Utnes. A prediction system for local wind variations in mountainous terrain. *Boundary-Layer Meteorology*, 112:557–586, Jan 2004.
12. J. C. Kaimal and J. J. Finnigan. *Atmospheric boundary layer flows. Their structure and measurement*. Oxford University Press, 1994.